Supplemental Material for:

"A theoretical study of hybrid lead iodide perovskite homologous semiconductors with 0D, 1D, 2D and 3D structure"

Jingyu Qian, Qing Guo, Leijing Liu, Bin Xu and Wenjing Tian**

Computational methods 2

Electronic structures (1D-BAT, 1D-NUG and 2D-WOG) 7

The fill factor (FF) calculated by SLME 8

The Calculated bandgap and Optical bandgap 9

The K-point-mesh optimization 9

Finite element analysis results 10

The Refcodes of CCDC of selected perovskite homologous 13

A list of published 2D PHSCs 14

Types of 2D perovskite homologous 15

Computational methods

1. First-principles calculations

The crystalline structure optimization and electronic structure calculations of FOL, BAT, NUG, QEX, YUV, WOG, AKO, NIC,UMU, MAP and XOC were performed by VASP[1]. The projector-augmented wave (PAW) potentials[2] were used to describe the Electron−ion interactions and the electron exchange-correction function was described by the generalized gradient approximation (GGA) parametrized by Perdew−Burke−Ernzerhof (PBE) [3]. The cutoff energy was set as 500 eV. Firstly, we tested the numbers of the k-points which were needed to use in optimization and static computation steps, and we found 4 × 4 × 4 k-point meshes were enough for almost all materials, except XOC. For XOC, 8 × 8 × 8 k-point meshes were enough (Table S2). Secondly, we optimized the atomic positions fully until all components of the residual forces were smaller than 0.001 eV/Å. Thirdly, in static computation step, the convergence threshold for self-consistent-field (SCF) iteration was set as 10^{-6} eV and the optimized crystalline structures were used to get the total energies and the wave functions. Fourthly, the density of states (DOS) and band structures were calculated using the wave functions obtained in static computation step. The k-points were increased to ensure the convergence of DOS. 8 × 8 × 8 k-point meshes were used for almost all materials, except XOC. For XOC, 16 × 16 × 16 k-point meshes were used. The width of the gaussian smearing was set as 0.1 eV. For the band structure calculation, 20 k-points between high symmetric points were used.

2. Semiempirical calculations

The experimental optical band gap of halide perovskites ABX_3 was taken into calculation for the absorption spectrum, with the use of scissor operator.[4] We calculated the dielectric frequency spectra firstly with the cutoff energy of 500 eV and a 12 × 12 × 12 k-point mesh, and the imaginary part was determined by a summation over empty states in the following equation[5]:

$$\varepsilon_2(\omega) = \left(\frac{4\pi e}{m_e \omega}\right)^2 |\langle v|p|c\rangle|^2 \rho_{cv}(\hbar\omega)[f(E_v) - f(E_c)] \quad (1)$$

Where v represents valence bands and c represents conduction bands. The real part could be obtained by the Kramers-Kronig relation:

$$\varepsilon_1(\omega) = \frac{2}{\pi} P \int_0^\infty \frac{\omega' \varepsilon_2(\omega')}{\omega'^2 - \omega^2} d\omega \quad (2)$$

In which P denotes the principal value. The frequency dependent absorption coefficient was then given by:

$$\alpha(\omega) = \omega\sqrt{\frac{-\varepsilon_1(\omega) + \sqrt{\varepsilon_1^2(\omega) + \varepsilon_2^2(\omega)}}{2}} \quad (3)$$

3. Shockley-Queisser Maximum Solar Cell Efficiency (S-Q)[6].

The standard AM1.5G and AM0 solar spectrum were used to calculate the efficiency. The I—V curve under illumination was described as $I=I_{sh}+I_0[1-\exp(qV/kT_c)]$, where I_{sh} is the short circuit current, I_0 is the reverse saturation current, V is the voltage between electrodes, T_c is the temperature of the solar cell, k is Boltzmann constant, and q is electronic charge. Ish was calculated by $I_{sh} = q\int_{E_g}^{\infty} I_{sun}(E)dE$, where E_g is the bandgap of material, and $I_{sun}(E)$ the sunlight photon flux at energy E. I_0 was calculated by $I_0 = q\int_{E_g}^{\infty} I_{bb}(E, T_c)dE$, where $I_{bb}(E,T_c)$ is the black-body spectrum at temperature T_c.

4. Spectroscopic Limited Maximum Efficiency (SLME)[7].

Developed from S-Q, the SLME method takes the photon absorptivity $\alpha_{abs}(E)$ into account. In this case, $I_{sh} = q\int_0^{\infty} \alpha_{abs}(E)I_{sun}(E)dE$ and $I_0 = q\int_0^{\infty} \alpha_{abs}(E)I_{bb}(E, T_c)dE$.

5. Polycrystalline model[8, 9]

In order to build a polycrystalline model, we set a box with dimensions of 250 × 250 × 250 nm firstly. Secondly, 50 random points were created and every point owned its independent coordinate system. Thirdly, we took these 50 points as crystal nucleuses and let them grow with the same speed at the same time. When the edge of one crystal nucleus met with that of another crystal nucleus, this crystal nucleus stopped growing in this direction. Finally, when there were no space for crystal nucleuses to grow, the polycrystalline model was built completely.

6. Finite element analysis[10, 11]

The material were divided into small cube element, and a simulated voltage was loaded along x axis. In order to calculate the electric current density on the faces (Γ_1) loaded voltage, the electric potential φ of every point in the model should be solved. According to the continuity equation of an electric current, the electric potential φ should meet the boundary conditions:

$$\left.\begin{aligned} &\iiint_V \nabla \bullet \sigma(-\nabla\varphi)dv = 0 \quad in \quad V \\ &\varphi = \varphi_0 \quad on \quad \Gamma_1 \\ &\frac{\partial\varphi}{\partial n} = 0 \quad on \quad \Gamma_2 \end{aligned}\right\} \quad (4)$$

Where known quantities σ mean the conductivities of elements in the model, Γ_2 means the other four faces except Γ_1. On Γ_2, the normal component of electric current is 0, so the electric field intensity perpendicular to Γ_2 (δφ/δn) is 0.

The calculus of variations were used to solve eq. 4:

$$\left.\begin{aligned} &\frac{1}{2}\iiint_V \sigma(-\nabla\varphi)^2 dv = \min \quad in \quad V \\ &\varphi = \varphi_0 \quad on \quad \Gamma_1 \end{aligned}\right\} \quad (5)$$

In order to solve eqution 5, the model was dispersed to N_e elements, every element is a cube with 20 nodes. A Piece-wise interpolation function of electric potential was introduced in every element, so every point in the element can be described by the electric potential of nodes and the corresponding shape function. The Gauss integration can be described as the element matrix. Finally, a system of linear algebraic equations can be build with the unknown electric potential of nodes:

$$K\varphi = 0 \quad (6)$$

where $K = \sum_1^{N_e} K_e$, and the element stiffness matrix

$$K_e = nq\iiint_{V_e}(\mu_{e,x}\frac{\partial N_i}{\partial x}\frac{\partial N_j}{\partial x} + \mu_{e,y}\frac{\partial N_i}{\partial y}\frac{\partial N_j}{\partial y} + \mu_{e,z}\frac{\partial N_i}{\partial z}\frac{\partial N_j}{\partial z})dv \quad (7)$$

where n is carrier concentration (set as $2.5*10^{17}$ m^{-3} in this article), q is electron charge and μ is carrier mobility.

The electric current density of each element: $$J_e = nq\mu_{e,x}\frac{\partial \varphi_e}{\partial x}$$

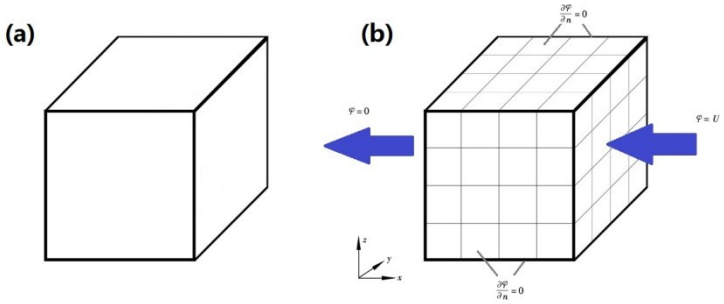

Fig. S1 The material (a) were divided into small cube element(b).

7. Formation energy[12]

Formation energies were calculated as:

$$E = \frac{E_{(PbI_2)_n(MI)_m} - nE_{PbI_2} - mE_{MI}}{n}$$

Where $E_{(PbI2)n(MI)m}$ is the total energy of the unit cell, E_{PbI2} is the average energy of one lead atom with two iodine atoms in the PbI_2 crystal at room temperature and E_{MI} is the energy of organic component MI at gas phase.

8. Effective masses calculation

We compared the difference between the second-order partial derivative method and the polynomial fitting (Fig. S2b). The electron effective mass of 2D-UMU is taken as an example (Fig. S2a). If we use common partial derivative method (Fig. S2c), the first-order partial derivative values at the endpoints produce error. Because the partial derivative values (f') is calculated as $(f'_{left}+f'_{right})/2$ for k_1, k_2 and k_3, but f' is calculated as $f'=f'_{right}$ for k_4 and $f'=f'_{left}$ for G, and the error will error transfer to the second-order partial derivative values (Table S1). We improved the second-order partial derivative method (Fig. S2d), by add the mirror points (k_1',k_2',k_3' and k_4') according to the high symmetric point (G) before taking the derivative (Table S2). By using our improved the second-order partial derivative method, the result is in accordance with that obtained from the polynomial fitting.

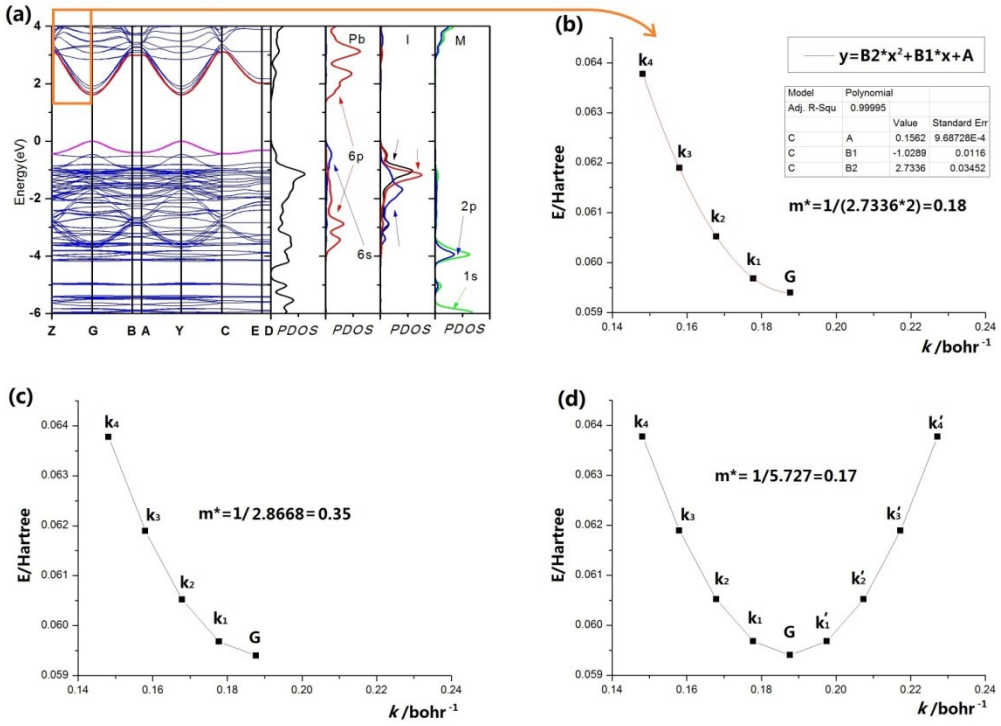

Fig. S2 The electronic structure of 2D-UMU (a). Effective masses calculated by the polynomial fitting (b). Effective masses calculated by the common second-order partial derivative method (c). Effective masses calculated by the improved second-order partial derivative method (d).

Table S1. Effective masses calculated by the common second-order partial derivative method

	k/bohr^{-1}	E/Hartree	first derivative		second derivative	
$\mathbf{k_4}$	0.1482	0.0638	-0.1902	error	2.5799	error
$\mathbf{k_3}$	0.1580	0.0619	-0.1647	TRUE	3.9525	error
$\mathbf{k_2}$	0.1679	0.0605	-0.1121	TRUE	5.4713	TRUE
$\mathbf{k_1}$	0.1778	0.0597	-0.0566	TRUE	4.2421	error
G	0.1877	0.0594	-0.0283	error	2.8668	error

Table S2. Effective masses calculated by the improved second-order partial derivative method

	k/bohr^{-1}	E/Hartree	first derivative		second derivative	
$\mathbf{k_4}$	0.1482	0.0638	-0.1902	error	2.5799	error
$\mathbf{k_3}$	0.1580	0.0619	-0.1647	TRUE	3.9525	error

$\mathbf{k_2}$	0.1679	0.0605	-0.1121	TRUE	5.4713	TRUE
$\mathbf{k_1}$	0.1778	0.0597	-0.0566	TRUE	5.6733	TRUE
G	0.1877	0.0594	0.0000	TRUE	5.7270	TRUE
$\mathbf{k_1'}$	0.1975	0.0597	0.0566	TRUE	5.6683	TRUE
$\mathbf{k_2'}$	0.2074	0.0605	0.1120	TRUE	5.4706	TRUE
$\mathbf{k_3'}$	0.2173	0.0619	0.1647	TRUE	3.9546	error
$\mathbf{k_4'}$	0.2272	0.0638	0.1902	error	2.5799	error

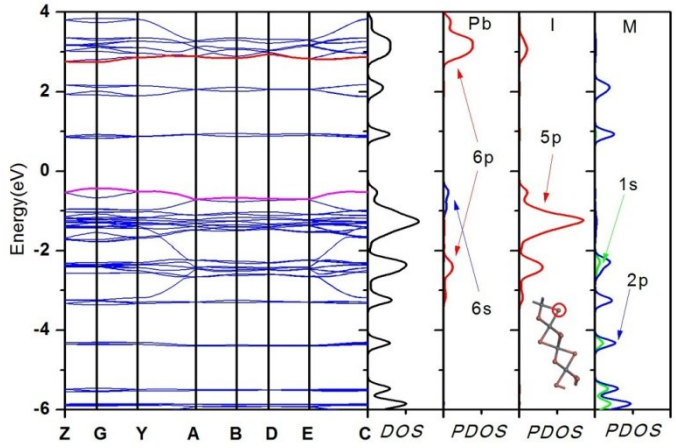

Fig. S3 Density of states (DOS), partial densities of states (PDOS) and band structures of 1D-BAT.

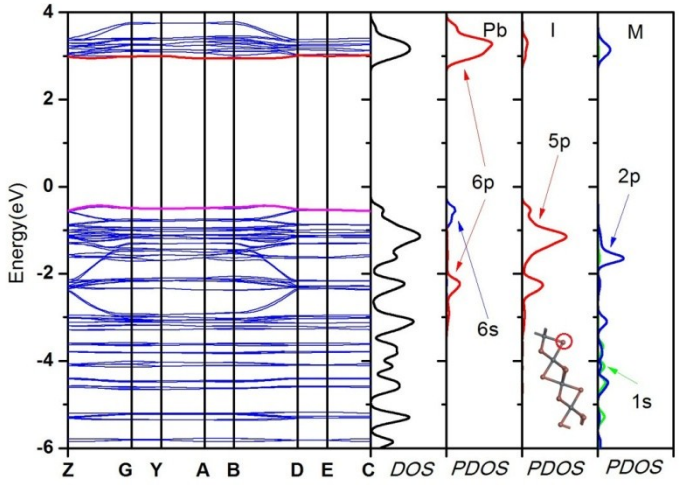

Fig. S4 Density of states (DOS), partial densities of states (PDOS) and band structures of 1D-NUG.

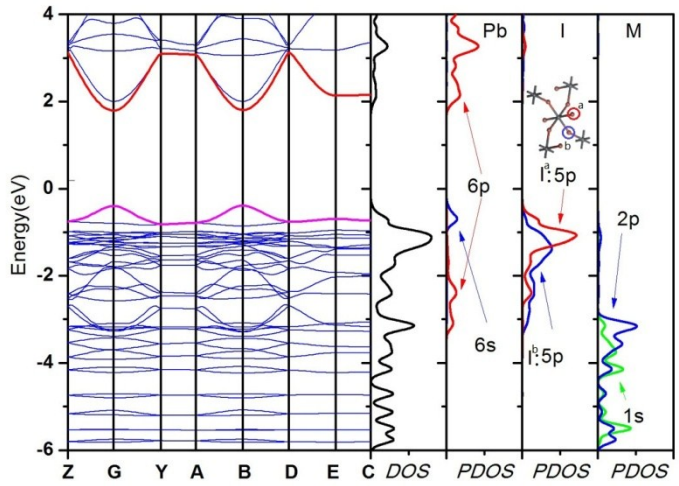

Fig. S5 Density of states (DOS), partial densities of states (PDOS) and band structures of 2D-WOG.

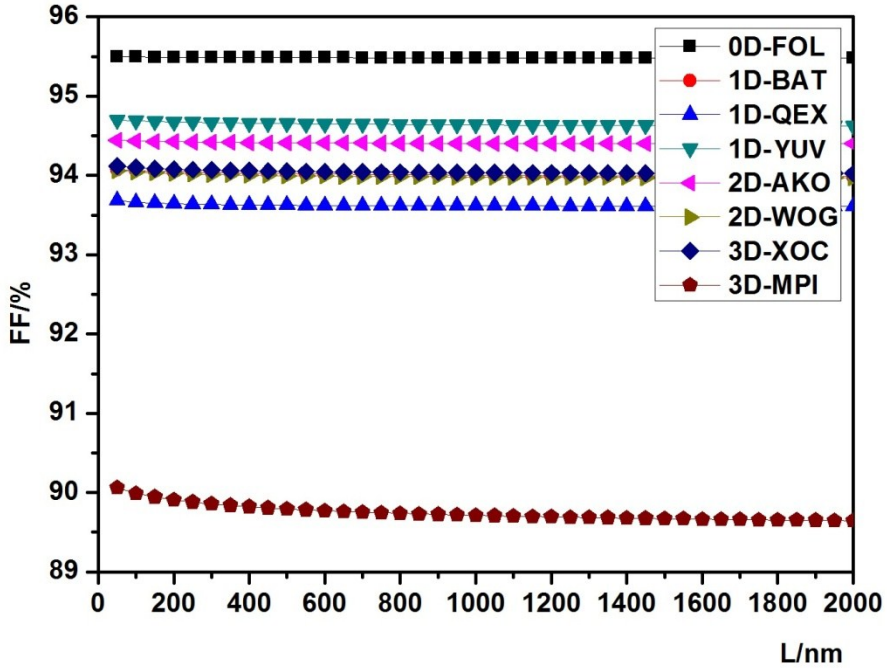

Fig. S6 The fill factor (FF) for 0D-FOL, 1D-BAT, 1D-QEX, 1D-YUV, 2D-AKO, 2D-WOG, 3D-XOC and 3D-MAP.

Table S3. The calculated bandgap and optical bandgap.

		Our Work	
Structure	ID	Calculated bandgap GGA/PBE (eV)	Optical bandgap(eV)
0 D	FOL	3.06	3.87[a]
1 D	NUG	3.38	——
1 D	BAT	3.18	2.71[b]
1 D	QEX	3.37	2.56[c]
1 D	YUV	2.32	3.18[h]
2 D	AKO	2.07	2.98[d]
2 D	NIC	1.91	——

2 D	WOG	2.19	2.73[e]
2 D	UMU	1.62	——
3 D	XOC	1.92	2.76[f]
3 D	MAP	1.47	1.52[g]

		Other's Work		
Structure	chemical formula	Calculated bandgap GGA/PBE (eV)	HSE+SOC(eV)	Optical bandgap(eV)
2 D	$CH_3(CH_2)_3NH_3PbI_4$	2.2[i]	1.96[i]	2.57[j]
3 D	$CH_3NH_3PbI_3$	1.57[k]	1.6[k]	1.52

a. reported by G. C. Papavassiliou et al.[13] b. reported by H. H. Li et al.[14] c. reported by et al.[15] d. reported by K. Pradeesh et al.[16] e. reported by G. A. Mousdis et al.[17] f. reported by H. H. Li et al.[18] g. reported by C. C. Stoumpos et al.[19] h. reported by I. B. Koutselas et al.[20] i. reported by L. Ma et al. [21] j. reported by T. Ishihara et al. [22] k. reported by S. H. Wei et al. [23]

Table S4. The K-point-mesh optimization.

Structure	ID	K-point	Energy(eV)
0 D	FOL	2*2*2	-404.845
		4*4*4	-404.866
1 D	NUG	2*2*2	-690.025
		4*4*4	-690.034
1 D	BAT	2*2*2	-389.663
		4*4*4	-389.667
1 D	QEX	2*2*2	-502.730
		4*4*4	-502.736
1 D	YUV	4*4*4	-565.603
2 D	AKO	2*2*2	-501.895
		4*4*4	-501.911
2 D	NIC	2*2*2	-279.177
		4*4*4	-279.178
2 D	WOG	2*2*2	-304.063
		4*4*4	-304.071
2 D	UMU	4*4*4	-971.259
3 D	XOC	2*2*2	-309.924
		4*4*4	-309.368
		8*8*8	-309.335
3D	MAP	2*2*2	-203.217
		4*4*4	-203.227

Table S5. One of the finite element analysis results for the current density of every nodes with carrier mobilities in a, b and c directions are 0.1, 10 and 0.1 $cm^2V^{-1}s^{-1}$. The relationship of current density for node number and the average electric current density is show in Fig. S7.

Node Number	X	Y	Z	Current Density (*10^{-3} mA/cm^2)
75776[a]	0	3.90E-02	2.70E-02	1870.3
75836[a]	0	4.00E-02	2.70E-02	5354.2
75898[a]	0	4.00E-02	2.60E-02	10156
75837[a]	0	3.90E-02	2.60E-02	60.578
75177[a]	0	2.80E-02	2.90E-02	2357.4
75176[a]	0	2.80E-02	3.00E-02	809.51
75214[a]	0	2.90E-02	3.00E-02	953.11
75215[a]	0	2.90E-02	2.90E-02	1300.8
75603[a]	0	3.60E-02	3.20E-02	617.5
75604[a]	0	3.60E-02	3.30E-02	685.4
75657[a]	0	3.70E-02	3.30E-02	1235.9
75658[a]	0	3.70E-02	3.20E-02	783.41
[a]		…		
545742[b]	1.00E-03	3.35E-02	1.60E-02	13256
547103[b]	1.00E-03	2.10E-02	2.65E-02	940.76
549277[b]	1.00E-03	2.20E-02	2.65E-02	2039.1
547105[b]	1.00E-03	2.15E-02	2.60E-02	1713.7
546790[b]	1.00E-03	1.70E-02	2.25E-02	559.64
546897[b]	1.00E-03	1.75E-02	2.30E-02	629.7
546894[b]	1.00E-03	1.80E-02	2.25E-02	1168.6
546787[b]	1.00E-03	1.75E-02	2.20E-02	1098.5
[b]		…		

[a] the nodes outside the polycrystalline model.

[b] the nodes inside the polycrystalline model.

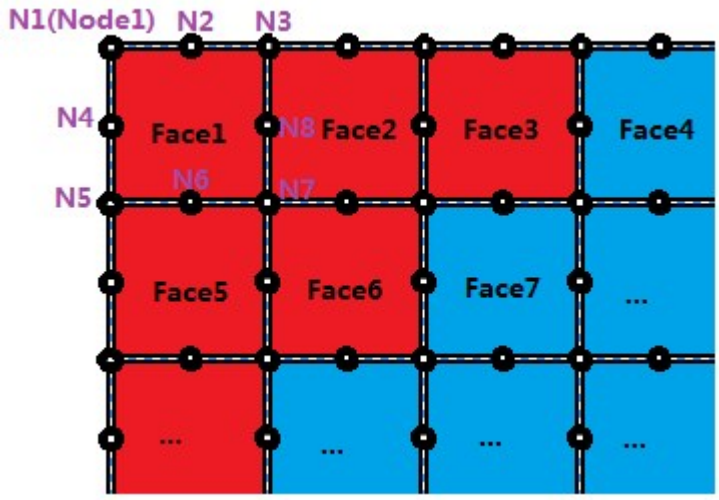

Fig. S7. The schematic diagram for the element chosen as a cube with 20 nodes outside the polycrystalline model (x=0). The current density (J) for the Face1 is calculated as $J_{Face1}=1/8*J_{N1}+1/4*J_{N2}+1/8*J_{N3}+1/4*J_{N4}+1/8*J_{N5}+1/4*J_{N6}+1/8*J_{N7}+1/4*J_{N8}$. The average electric current density listed in Table S4 and Table S5 is calculated as $J_{av.}=(J_{Face1}+J_{Face2}+...+J_{FaceN})/N$. The red part and blue part means different crystalline grains in the polycrystalline model.

Table S6. 50 parallel tests for the average electric current density ($*10^{-3}$ mA/cm^2) changed with the the carrier mobility in b direction decreases from 10^{-1} to 10^{-2} to 10^{-3} to 10^{-4} (data have been sorted from smallest to biggest)

serial number	carrier mobilities in a, b and c directions/cm^{2}V^{-1}s^{-1}			
	$10:10^{-1}:10$	$10:10^{-2}:10$	$10:10^{-3}:10$	$10:10^{-4}:10$
1	3793	887	322	95
2	3808	1123	335	98
3	3856	1139	349	108.73
4	3896	1140	363	113
5	3918	1177.18	371	128.93
6	3956.17	1239.06	396.89	129.5
7	4127.9	1324	412.25	135.55
8	4130	1333.79	417.86	158.18
9	4140.42	1335	440.55	158.43
10	4254	1356.24	478	165
11	4441.354	1434	510	167
12	4466.18	1437	516.85	173
13	4551.41	1468	542	187.37
14	4566	1517	549.12	198
15	4573.78	1520	552	223
16	4610.26	1613.57	576	241
17	4610.42	1747.64	597	267
18	4618	1780	770	276

19	4648	1787.92	784	279
20	4671	1789.77	812.38	305
21	4691	1790	817.33	307
22	4704	1867.39	820.5	338.5
23	4722.11	1909.88	826	339
24	4731	1950	849	339.6
25	4816.3	1955	864	343.92
26	4841	2008	886	350.89
27	4897	2016.123	948.944	413
28	4925.27	2050.29	961.86	431
29	5239	2059	977.25	461
30	5257	2105	1033.87	532.76
31	5269	2126	1038	550
32	5270	2152	1052.6	550
33	5402	2164	1095	586
34	5514	2322	1114.33	592
35	5767.9	2340.64	1117	613
36	5923	2360.322	1124	704.18
37	5971	2432	1147.37	709.12
38	5974.68	2435.06	1158	839.76
39	6003	2457	1270	845.32
40	6038	2536	1292	852.24
41	6057.78	2545	1300	854.8
42	6121	2679	1336.2	967
43	6164	2732.5	1339.44	1007
44	6335	2761	1418	1049
45	6470	2766	1482	1135.46
46	6597.07	2817	1516	1151
47	6760	2959	1644	1391
48	6772	3048	1657	1394
49	7389.22	3051	1785.87	1514
50	12612.32	3549.38	1901	1716

Table S7. 50 parallel tests for the average electric current density (*10^{-3} mA/cm^2) changed with the the carrier mobility in a and c direction decreases from 10^{-1} to 10^{-2} to 10^{-3} to 10^{-4} (data have been sorted from smallest to biggest)

serial	carrier mobilities in a, b and c directions/cm^{2}V^{-1}s^{-1}			
number	10^{-1}:10:10^{-1}	10^{-2}:10:10^{-2}	10^{-3}:10:10^{-3}	10^{-4}:10:10^{-4}
1	7351	5625	4356	1375
2	7887	6112	5360	1817
3	8315.59	6254	5414	1849.6
4	8346.77	6557.13	5529.66	1884

5	8385	6660	5653.65	1921.7
6	8445	6833	5684	1953
7	8698	7340	5754	2072
8	8750.64	7350.8	5870	2140.989
9	8827	7457	6213.019	2146.45
10	8980.988	7468	6267	2261
11	9087	7482	6294.817	2290
12	9204	7601.5	6334	2347
13	9243.05	7752.24	6393.22	2362
14	9319.8	7924	6531	2448.578
15	9337	7933	6568	2509
16	9582	7939	6615	2528
17	9641	8226	6615.82	5330
18	9750	8238.598	6838	5844
19	9818.23	8257	6838.2	6267.155
20	9842	8325	7095	6364
21	10039	8400	7106.43	6591
22	10084	8434.98	7129.172	7079.367
23	10215	8665	7180	7161
24	10282.56	8670	7221	7192
25	10544	8729	7284.33	7264.26
26	10708	8875	7634	7602
27	10776	9161.27	8006.24	7981.43
28	10778.39	9247.212	8024	7997
29	10800	9349	8056	8036
30	10829.38	9361	8150	8123
31	10894	9410	8470	8449
32	10957.4	9498.83	9167	9151
33	11018.23	9500	9234	9215
34	11050	9542	9311.66	9293.46
35	11051	9562.94	9360	9341
36	11126	9643.98	9441.3	9418.787
37	11191.65	9728	9500	9475
38	11235	9974	9791	9771
39	11334.77	10089.41	9909.653	9892.9
40	11362.9	10212	10016	9999
41	11421	10220.7	10056	10033.98
42	11428	10251	10081	10047
43	11447	10388	10086	10064
44	11455	10390	10207	10188
45	11542	10530	10375	10359
46	11792	10839.06	10654.64	10634.4
47	11975.02	10978	10824	10805

48	12127.28	11196.26	11028.36	11011.27
49	12255.35	11253.05	11073	11047
50	12426	11304	11112.2	11097.18

Table S8. The Refcodes of CCDC of selected perovskite homologous.

Structure	ID	Refcode (CCDC)
0 D	FOL	FOLLIB01
1 D	NUG	NUGLOR
1 D	BAT	BATBIJ
1 D	QEX	QEXSIW
1 D	YUV	YUVFOK
2 D	AKO	AKOBUY
2 D	NIC	NICYEE02
2 D	WOG	WOGJEH
2 D	UMU	UMUBUB01
3 D	XOC	XOCNEJ
3 D	MAP	MAPBTI04

Table S9. A list of published 2D PHSCs.

Perovskites homologous	Bandgap(eV)	PCE(%)
$MAPbI_3$	1.52	19.10%[24]
$(MA,FA,Cs)PbI_3$	1.50	21.10%[25]
$FAPbI_3$	1.48	20.10%[26]
$(HA)_2PbI_4$	2.57	1.10%[27]
$(PEA)_2PbI_4$	2.34	0.15%[28]
BA_2PbI_4	2.30	0.12%[29]
BA_2PbI_4	2.25	0.60%[30]
$(PEA)_2(MA)Pb_2I_7$	2.13	1.19%[28]
$(PEA)_2(MA)Pb_2I_7$	2.13	3.72%[28]
$BA_2CsPb_2I_7$	1.72	4.84%[29]
$BA_2(MA)Pb_2I_7$	1.85	2.00%[30]
$(PEA)_2(MA)_2Pb_3I_{10}$	1.94	1.62%[28]
$(PEA)_2(MA)_2Pb_3I_{10}$	2.06	4.73%[31]
$(BA)_2(MA)_2Pb_3I_{10}$	2.04	4.02%[32]

$(PEI)_2(MA)_2Pb_3I_{10}$	1.95	4.23%[33]
$BA_2(MA)_2Pb_3I_{10}$	1.70	11.40%[34]
$(BA)_2(MA)_3Pb_4I_{13}$	1.62	11.60%[34]
$BA_2(MA)_3Pb_4I_{13}$	1.62	12.30%[30]
$BA_2(MA)_3Pb_4I_{13}$	1.62	2.40%[32]
$(PEI)_2(MA)_4Pb_5I_{16}$	1.80	6.98%[33]
$(PEI)_2(MA)_6Pb_7I_{22}$	1.70	9.39%[33]
$(CH_3(CH_2)_3NH_3)_2(CH_3NH_3)_4Pb_5I_{16}$	1.55	8.71%[34]
$(PEA)_2(MA)_{39}Pb_{40}I_{121}$	1.55	16.00%[12]
$(BA)_2(MA)_4Pb_5I_{16}$	1.62	9.20%[30]
$(BA)_2$ $(MA)_{59}Pb_{60}I_{181}$	1.61	15.40%[35]

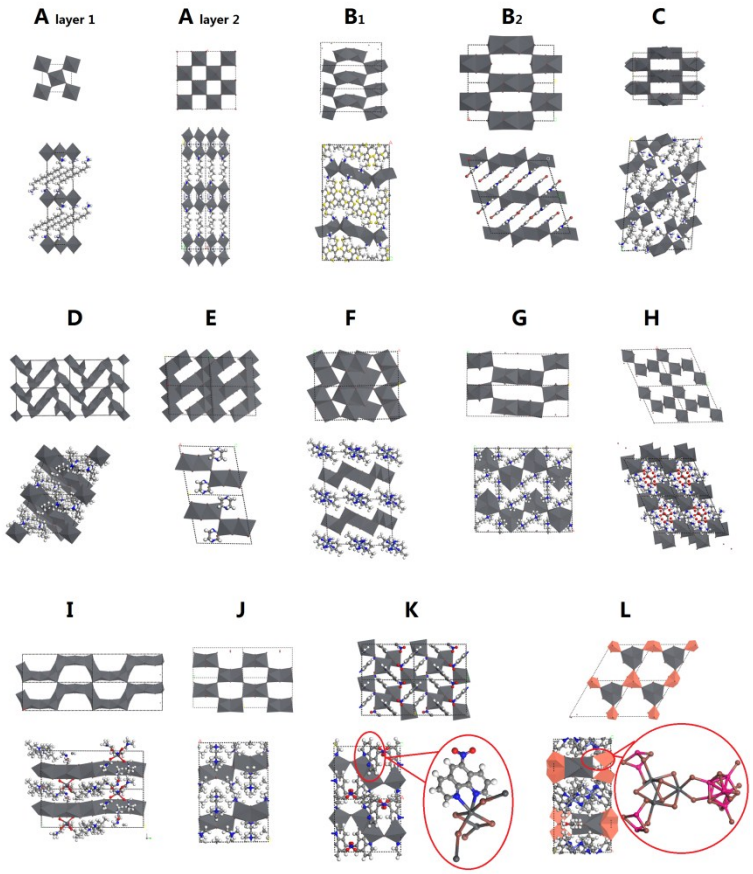

Fig. S8. Types of 2D perovskite homologous.

Table S10. A list of published 2D perovskite homologous (before 2017-2).

Refcode	Ty	lay	Organic complex ion

	pe	er	
AKOBUY	A	1	Dodecane-1,12-diaminium
AKOBUY01	A	1	Dodecane-1,12-diaminium
BAYHAL	A	1	2,2'-(6H,6'H-[2,2'-bithiopyran]-5,5'-diylbis(sulfanediyl))bis(ethan-1-aminium)
CELBUR	A	1	2-Cyclohexyl-ethylaminium
COTVIQ	A	1	Benzylaminium
DESFUD	A	1	1-Phenyl-ethylaminium
DESGAK	A	1	1-Phenyl-ethylaminium
FIXMOP	A	1	4-Chloro-phenylaminium
FIXMOP01	A	1	4-Chloro-phenylaminium
GOMLAW	A	1	4-iodobenzenaminium
JIMDEO	A	1	1-Phenyl-ethyl-ammonium
JIMDEO01	A	1	1-Phenyl-ethyl-ammonium
KECKOS	A	1	nonan-1-aminium
KECKOS01	A	1	nonan-1-aminium
KECKOS02	A	1	nonan-1-aminium
LASFAO	A	1	butane-1,4-diaminium
LASFIW	A	1	octane-1,8-diaminium
LASGAP	A	1	naphthalene-1,5-diaminium
MEMXUX	A	1	p-tolylmethanaminium
MUBHIA	A	1	(1l4,3-dithiol-2-yl)methanaminium
NAVSEK	A	1	heptan-1-aminium
NAVSEK01	A	1	heptan-1-aminium
NAVTUB02	A	1	decan-1-aminium
NAVTUB03	A	1	decan-1-aminium
NAVTUB04	A	1	decan-1-aminium
NAVTUB05	A	1	decan-1-aminium
NICYEE	A	1	2-hydroxyethan-1-aminium
NICYEE02	A	1	2-hydroxyethan-1-aminium

NUXHAQ	A	1	3-hydroxypropan-1-aminium
NUXHIY	A	1	3-iodopropan-1-aminium
NUXHOE	A	1	4-iodobutan-1-aminium
NUXHUK	A	1	5-iodopentan-1-aminium
NUXJAS	A	1	6-iodohexan-1-aminium
NUXJIA01	A	1	2,2'-disulfanediylbis(ethan-1-aminium)
QARWOW	A	1	3-carboxypropan-1-aminium
QUFBUO	A	1	1H,1'H-[2,2'-biimidazole]-3,3'-diium
SILTIR	A	1	pentan-1-aminium
SILTIR01	A	1	pentan-1-aminium
SILTIR02	A	1	pentan-1-aminium
SILTOX	A	1	hexan-1-aminium
SILTOX01	A	1	hexan-1-aminium
TECFAI	A	1	butan-1-aminium
TECFAI01	A	1	butan-1-aminium
TECFAI02	A	1	butan-1-aminium
TEYMIU	A	1	2-iodoethan-1-aminium
TEYMIU02	A	1	2-iodoethan-1-aminium
TEYMOA	A	1	2-bromoethan-1-aminium
TEYMOA01	A	1	2-bromoethan-1-aminium
TEYMOA04	A	1	2-bromoethan-1-aminium
TEYMUG	A	1	2-chloroethan-1-aminium
VEZNEU	A	1	cyclopropanaminium
VEZNIY	A	1	cyclobutanaminium
VEZNOE	A	1	cyclopentanaminium
VEZNUK	A	1	cyclohexanaminium
VUHDAE	A	1	2-cyanoethan-1-aminium
VUYKAC	A	1	cyclohexane-1,4-diyldimethanaminium
WOGJEH	A	1	hexane-1,6-diaminium
WOLNIV	A	1	dodecan-1-aminium
WOLNIV01	A	1	dodecan-1-aminium
WOLNOB	A	1	tetradecan-1-aminium
WOLNOB01	A	1	tetradecan-1-aminium

WOLNUH	A	1	hexadecan-1-aminium
WOLNUH01	A	1	hexadecan-1-aminium
WOLPAP	A	1	octadecan-1-aminium
WOLPAP01	A	1	octadecan-1-aminium
RUZQEK	A	1	(4-chlorophenyl)methanaminium
ETUBUS	A	1	2-(thiophen-2-yl)ethan-1-aminium
LASFIW01	A	1	octane-1,8-diaminium
UXEREW	A	1	3-bromopyridin-1-ium
VEZNUK01	A	1	cyclohexanaminium
VEZNUK02	A	1	(1S)-cyclohexane-1,2-diaminium
WOGJEH02	A	1	hexane-1,6-diaminium
BARHOU	A	1	2-phenylethan-1-aminium
CAPYAW	A	1	cyclohexanaminium
CAPYAW01	A	1	cyclohexanaminium
COTVIQ02	A	1	phenylmethanaminium
IBOJUH	A	1	1H-benzo[d]imidazol-3-ium
NUXJAS01	A	1	6-iodohexan-1-aminium
UCUQOB	A	1	4-(2-ammonioethyl)-1H-imidazol-3-ium
UXEREW02	A	1	3-bromopyridin-1-ium
JIMDIS	A	2	2-phenylethan-1-aminium;methanaminium
MEMYAE	A	2	p-tolylmethanaminium;methanaminium
MUBHEW	A	2	(1l4,3-dithiol-2-yl)methanaminium;methanaminium
QARWIQ	A	2	3-carboxypropan-1-aminium;methanaminium
UMUBUB	A	2	butan-1-aminium;methanaminium
UMUBUB01	A	2	butan-1-aminium;methanaminium
ROZZAJ	A	3	2-phenylethan-1-aminium;methanaminium
UMUCAI	A	3	butan-1-aminium;methanaminium
UMUCAI01	A	3	butan-1-aminium;methanaminium

UMUCEM	A	4	butan-1-aminium;methanaminium
UMUCEM01	A	4	butan-1-aminium;methanaminium
UXENOC02	B1		4-bromopyridin-1-ium
UXESOH02	B1		4-chloropyridin-1-ium
WEHSAE	B1		3-phenylpropan-1-aminium
UXENOC	B1		4-bromopyridin-1-ium
UXESOH	B1		4-chloropyridin-1-ium
BAYHEP	B1		2-([2,2'-bithiophen]-5-ylthio)ethan-1-aminium
IGECIG	B1		2-benzylisothiouronium
UXENIW02	B2		3-bromopyridin-1-ium
CEWCEN	H		Ethane-1,2-diaminium;Oxalic acid
LORKAG	K		2-(quinolin-8-yloxy)acetate
MUPQUK	K		1,10-phenanthroline
EBUQEZ	K		5-nitro-1,10-phenanthroline
EBUQOJ	K		5-chloro-1,10-phenanthroline
GEQGUE	I		N1,N1,N1,N2,N2,N2-hexapropylethane-1,2-diaminium;N,N-dimethylformamide;
GEQHAL	J		N1,N1,N1,N2,N2,N2-hexamethylethane-1,2-diaminium
KEXCAS	L		1,10-phenanthroline;ethanol
LERGIY	D		N1,N1,N1,N5,N5,N5-hexapropylpentane-1,5-diaminium
PARZIT	E		1,4-diazabicyclo[2.2.2]octane
QOWQOJ	F		benzene-1,2-diamine;acetonitrile
TIDVOR	G		N1,N1,N1,N3,N3,N3-hexamethylpropane-1,3-diaminium
TILNOS	G		N1,N1,N1,N2,N2,N2-hexamethylethane-1,2-diaminium
GEHPEP	C		Propylaminium

[1] G. Kresse, J. Furthmüller, ller : Efficient iterative schemes for ab initio total-energy calculations using a plane-wave basis set, Phys. Rev. B, 54 (1996) 11169-11186.
[2] B. PE, Projector Augmented-Wave Method, Phys. Rev. B, 50 (1994) 17953-17979.
[3] J.P. Perdew, K. Burke, M. Ernzerhof, Generalized gradient approximation made simple, Phys. Rev. Lett., 77 (1996) 3865-3868.
[4] W.J. Yin, T. Shi, Y. Yan, Unique properties of halide perovskites as possible origins of the superior solar cell performance, Adv. Mater., 26 (2014) 4653-4661.

[5] P. Umari, E. Mosconi, F. De Angelis, Relativistic GW calculations on CH3NH3PbI3 and CH3NH3SnI3 Perovskites for Solar Cell Applications, Sci. Rep., 4 (2014) 4467-4467.
[6] W. Shockley, H.J. Queisser, Detailed Balance Limit of Efficiency of p-n Junction Solar Cells, J. Appl. Phys., 32 (1961) 510-519.
[7] L.P. Yu, A. Zunger, Identification of Potential Photovoltaic Absorbers Based on First-Principles Spectroscopic Screening of Materials, Phys. Rev. Lett., 108 (2012) 1-5.
[8] W.M. Ashmawi, M.A. Zikry, Single void morphological and grain-boundary effects on overall failure in F.C.C. polycrystalline systems, Materials Science & Engineering A, 343 (2003) 126–142.
[9] M.T.D. Berg, M.J.V. Kreveld, M.H. Overmars, O. Schwarzkopf, Computational Geometry: Algorithms and Applications (second edition), (2000).
[10] H. Lin, Three-dimensional finite element analysis for electrical conductivity of electro-contact alloy material, Journal of Southeast Univwrsity, 32 (2002) 627-630.
[11] C. Liu, J. He, J. Zou, 3-dimensional simulation on electrical conductivity of CuCr contactmaterials, International Symposium on Discharges and Electrical Insulation in Vacuum, 2000. Proceedings. Isdeiv2000, pp. 733-737 vol.732.
[12] L.N. Quan, M. Yuan, R. Comin, O. Voznyy, E.M. Beauregard, S. Hoogland, A. Buin, A.R. Kirmani, K. Zhao, A. Amassian, D.H. Kim, E.H. Sargent, Ligand-Stabilized Reduced-Dimensionality Perovskites, J. Am. Chem. Soc., 138 (2016) 2649-2655.
[13] G.C. Papavassiliou, I.B. Koutselas, Structural, optical and related properties of some natural three- and lower-dimensional semiconductor systems, Synth. Met., 71 (1995) 1713-1714.
[14] H.-H. Li, Y.-J. Wang, Z.-X. Lian, Y.-F. Xu, M. Wang, S.-W. Huang, Z.-R. Chen, An additional structure and property study on polymeric haloplumbates(II) with aromatic N-heterocyclic organic molecules, J. Mol. Struct., 1016 (2012) 118-125.
[15] S. Elleuch, Y. Abid, A. Mlayah, H. Boughzala, Vibrational and optical properties of a one-dimensional organic–inorganic crystal [C6H14N]PbI3, J. Raman Spectrosc., 39 (2008) 786-792.
[16] K. Pradeesh, G.S. Yadav, M. Singh, G. Vijaya Prakash, Synthesis, structure and optical studies of inorganic–organic hybrid semiconductor, NH3(CH2)12NH3PbI4, Mater. Chem. Phys., 124 (2010) 44-47.
[17] G.A. Mousdis, G.C. Papavassiliou, C.P. Raptopoulou, A. Terzis, Preparation and characterization of [H3N(CH2)6NH3]PbI4 and similar compounds with a layered perovskite structure, J.mater.chem, 10 (2000) 515-518.
[18] H.H. Li, L.G. Sun, Z.R. Chen, Y.J. Wang, J.Q. Li, ChemInform Abstract: Incorporating a Transition Metal Complex into Polymeric Iodoplumbate: Structure Characterization, Properties and Theoretical Study of a Unprecedented Hybrid Semiconductor: {[Cu(en) 2][Pb 2 I 6]} n, Cheminform, 39 (2008) 391-396.
[19] C.C. Stoumpos, C.D. Malliakas, M.G. Kanatzidis, Semiconducting tin and lead iodide perovskites with organic cations: phase transitions, high mobilities, and near-infrared photoluminescent properties, Inorg. Chem., 52 (2013) 9019-9038.
[20] I.B. Koutselas, D.B. Mitzi, G.C. Papavassiliou, G.J. Papaioannou, H. Krautscheid, Optical and related properties of natural one-dimensional semiconductors based on PbI and SnI units, Synth. Met., 86 (1997) 2171-2172.
[21] L. Ma, J. Dai, X.C. Zeng, Two-Dimensional Single-Layer Organic-Inorganic Hybrid Perovskite Semiconductors, Advanced Energy Materials, 7 (2017) 1601731.
[22] T. Ishihara, Optical properties of PbI-based perovskite structures, J. Lumin., 60 (1994) 269-274.

[23] W.J. Yin, J.H. Yang, J. Kang, Y. Yan, S.H. Wei, Halide Perovskite Materials for Solar Cells: A Theoretical Review, J. Mater. Chem. A, 3 (2014) 8926-8942.
[24] C. Roldán-Carmona, P. Gratia, I. Zimmermann, G. Grancini, P. Gao, M. Graetzel, M.K. Nazeeruddin, High efficiency methylammonium lead triiodide perovskite solar cells: The relevance of non-stoichiometric precursors, Energ. Environ. Sci., 8 (2015) 3550-3556.
[25] S. Michael, M. Taisuke, S. Ji-Youn, D. Konrad, C.B. Juan-Pablo, N.M. Khaja, S.M. Zakeeruddin, T. Wolfgang, A. Antonio, H. Anders, Cesium-containing triple cation perovskite solar cells: improved stability, reproducibility and high efficiency††Electronic supplementary information (ESI) available. See DOI:10.1039/c5ee03874jClick here for additional data file, Energ. Environ. Sci., 9 (2016) 1989.
[26] W.S. Yang, J.H. Noh, N.J. Jeon, Y.C. Kim, S. Ryu, J. Seo, S.I. Seok, High-performance photovoltaic perovskite layers fabricated through intramolecular exchange, Science, 348 (2015) 1234-1237.
[27] L. Mao, H. Tsai, W. Nie, L. Ma, J. Im, C.C. Stoumpos, C.D. Malliakas, F. Hao, M.R. Wasielewski, A.D. Mohite, M.G. Kanatzidis, Role of Organic Counterion in Lead- and Tin-Based Two-Dimensional Semiconducting Iodide Perovskites and Application in Planar Solar Cells, Chem. Mater., 28 (2016) 7781-7792.
[28] X. Gan, O. Wang, K. Liu, X. Du, L. Guo, H. Liu, 2D homologous organic-inorganic hybrids as light-absorbers for planer and nanorod-based perovskite solar cells, Solar Energy Materials & Solar Cells, 162 (2017) 93-102.
[29] J.-F. Liao, H.-S. Rao, B.-X. Chen, D.-B. Kuang, C.-Y. Su, Dimension engineering on cesium lead iodide for efficient and stable perovskite solar cells, J. Mater. Chem. A, 5 (2017) 2066-2072.
[30] J.C. Blancon, H. Tsai, W. Nie, C.C. Stoumpos, L. Pedesseau, C. Katan, M. Kepenekian, C.M. Soe, K. Appavoo, M.Y. Sfeir, Extremely efficient internal exciton dissociation through edge states in layered 2D perovskites, Science, (2017).
[31] I.C. Smith, E.T. Hoke, D. Solisibarra, M.D. Mcgehee, H.I. Karunadasa, A layered hybrid perovskite solar-cell absorber with enhanced moisture stability, Angew. Chem., 53 (2014) 11232.
[32] D.H. Cao, C.C. Stoumpos, O.K. Farha, J.T. Hupp, M.G. Kanatzidis, 2D Homologous Perovskites as Light-Absorbing Materials for Solar Cell Applications, J. Am. Chem. Soc., 137 (2015) 7843.
[33] K. Yao, X. Wang, Y.-x. Xu, F. Li, L. Zhou, Multilayered Perovskite Materials Based on Polymeric-Ammonium Cations for Stable Large-Area Solar Cell, Chem. Mater., 28 (2016) 3131-3138.
[34] H. Tsai, W. Nie, J.C. Blancon, C.C. Stoumpos, R. Asadpour, B. Harutyunyan, A.J. Neukirch, R. Verduzco, J.J. Crochet, S. Tretiak, L. Pedesseau, J. Even, M.A. Alam, G. Gupta, J. Lou, P.M. Ajayan, M.J. Bedzyk, M.G. Kanatzidis, High-efficiency two-dimensional Ruddlesden-Popper perovskite solar cells, Nature, 536 (2016) 312-316.
[35] N.Q. Li, M. Yuan, R. Comin, O. Voznyy, E.M. Beauregard, S. Hoogland, A. Buin, A.R. Kirmani, K. Zhao, A. Amassian, Ligand-Stabilized Reduced-Dimensionality Perovskites, J. Am. Chem. Soc., 138 (2016) 2649.